Effects of dimerization on the photoelectron angular distribution parameters from chiral camphor enantiomers obtained with circularly polarized vacuum-ultraviolet radiation

Laurent Nahon,[1,*] Gustavo A. Garcia,[1] Héloïse Soldi-Lose,[1] Steven Daly,[2] and Ivan Powis[2,†]
[1]*Synchrotron SOLEIL, l'Orme des Merisiers, Saint Aubin Boîte Postale 48, 91192 Gif sur Yvette Cedex, France*
[2]*School of Chemistry, University of Nottingham, Nottingham NG7 2RD, United Kingdom*
(Received 20 July 2010; published 28 September 2010)

As an intermediate state of matter between the free monomeric gas phase and the solid state, clusters may exhibit a specific electronic structure and photoionization dynamics that can be unraveled by different types of electron spectroscopies. From mass-selected ion yield scans measured for photoionization of (*R*)-camphor, the ionization potentials (IPs) of the monomer (8.66 ± 0.01 eV), and of the homochiral dimer ($\leqslant 8.37 \pm 0.01$ eV) and trimer ($\leqslant 8.30 \pm 0.01$ eV) were obtained. These spectra, combined with threshold photoelectron spectroscopy and velocity map ion imaging, allow us to show that the camphor monomer and dimer photoionization channels are decoupled, i.e., that the highest occupied molecular orbital (HOMO) of the dimer does not undergo a dissociative ionization process that would lead to a spurious contribution to the monomer ion channel. Therefore mass selection, as achieved in our imaging photoelectron-photoion coincidence experiments, leads to size selection of the nascent monomer or dimer species. Since both the monomer and dimer are chiral, their photoelectron angular distribution (PAD) not only involves the usual β anisotropy parameter but also a chiral asymmetry parameter b_1 that can generate a forward-backward asymmetry in the PAD. This has been investigated using circularly polarized light (CPL) to record the photoelectron circular dichroism (PECD) in the near-threshold vacuum-ultraviolet (VUV) photoionization region. Analysis of size-selected electron images recorded with left- and right-handed CPL shows that over the first 1.5 eV above the HOMO orbital ionization potentials (IPs), the β parameter is not affected by the dimerization process, while the chiral b_1 parameter shows clear differences between the monomer and the dimer, confirming that PECD is a subtle long-range probe of the molecular potential.

DOI: 10.1103/PhysRevA.82.032514 PACS number(s): 33.60.+q, 33.55.+b, 36.40.−c

I. INTRODUCTION

The use of cooled molecular beams to generate clusters, and so to both bridge and extend the states of matter that can be investigated, is extremely well established [1,2]. Nevertheless, a persistent problem remains that of size selection, since typically in such a beam a range of cluster sizes are prepared, and so identifying properties of a specific cluster can become an issue. Photoionization spectroscopies offer a near-universal probing method for cluster systems with, in principle, many variants of the technique being possible. In particular electron-ion coincidence recording suggests a means for performing electron spectroscopy on mass-selected systems, although to achieve full, unambiguous size selection requires an assumption that the selected ion is a parent ion, and not some fragment of a larger cluster generated by dissociative photoionization.

Investigation of photoelectron angular distributions (PADs) extends the information available from photoelectron spectroscopy and so expands on the insights into target electronic structure and dynamics that may be gained from photoionization studies [3]. However, there are almost no instances of these approaches successfully applied to cluster systems, the exceptions being two recent reports [4,5] concerning inner-shell electron anisotropy of the rare gas dimers Ar_2 and Ne_2 and one further investigation which has examined valence-shell electron distributions from very large, non-size-selected rare gas clusters (mean $N \geqslant 500$) [6]. To our knowledge, no electron angular distribution measurements on directly size-selected molecular clusters or solvated (heterogeneous) cluster species have been reported.

In the present study our aim is to examine PADs from randomly oriented dimers of a medium-large natural product molecule, camphor ($C_{10}H_{16}O$). Since camphor is a chiral molecule, and hence its homodimer is also chiral, we are presented with an opportunity to examine not just the traditional electron anisotropy parameter β but also a second chiral asymmetry parameter b_1 that is accessible using the recent technique of photoelectron circular dichroism (PECD) [7] with circularly polarized light (CPL).

The general form of the predicted electron distribution for randomly oriented molecules and a specific polarization p[=0 for linear polarization, $= \pm 1$ for left (right) CPL], is

$$I(\theta) = 1 + b_1^{\{p\}} P_1(\cos\theta) + b_2^{\{p\}} P_2(\cos\theta),$$

where $b_2^{\{p\}}$ is directly proportional to the conventional β anisotropy parameter and $b_1^{\{p\}}$ will be zero for all but chiral molecules in combination with CPL. P_l are the Legendre polynomials, and θ the angle of electron emission with respect to the photon quantization axis, i.e., the photon axis in the case of CPL. The sign of b_1 will reverse if the handedness either of the molecular enantiomer or of the radiation is reversed (i.e., $p = +1 \leftrightarrow p = -1$), while the b_2 parameter will remain unaltered under such changes. This therefore predicts the PECD signal (difference of angular distributions recorded with left-handed and right-handed CPL) to be $2b_1\cos\theta$, i.e., a difference in photoelectron emission forward and backward along the light beam.

*laurent.nahon@synchrotron-soleil.fr
†ivan.powis@nottingham.ac.uk

Because of its intrinsic differential nature, PECD is allowed in the electric dipole ($E1$) approximation, which is not the case for CD in absorption. This then leads to very high relative asymmetry factors, ranging from a few to a few tens of percent, as has been measured and calculated for camphor [8–12] and several other types of chiral molecules in recent years [13–17]. Besides such astonishingly large chiral asymmetry, core- and valence-shell studies have shown that PECD is a strongly dynamical (final-state) effect showing a rich photon energy dependence [13] and also that it clearly depends on the ionized orbital (initial-state effect) [11]. In addition, PECD proves to be a very sensitive probe of molecular conformation [16,18] and of the chemical environment (chemical substitution) [19,20], much more so than the ionization cross section or the usual β parameter, this sensitivity appearing especially strong in the case of valence-shell PECD [21].

These characteristics, and the unprecedented magnitude of the chiral asymmetry, make PECD useful as a probe of fundamental ionization dynamics as well as permitting the identification of conformation and the determination of absolute chiral configuration when applied in combination with theoretical modeling—even in the case of a prototype floppy, multiconformer, orbitally congested system such as *endo*-borneol [17].

To date, experimental and theoretical studies of PECD have only been centered on pure enantiomers of free monomeric chiral species. We seek here to extend the scope of these works to study the effect of clustering, and especially dimerization, upon PECD, since it appears as a very sensitive, long-range probe of the whole molecular system. Hence, one might expect some specific cluster features, quite different from the case of the pure monomer. For instance, in the case of conventional CD, a dramatic amplification of the CD magnitude in absorption (up the percentage range) has been observed in chiral nanoparticles due to a local crystallization order enhancing the intrinsic chirality of the individual molecules [22,23]. One might wonder if a caging effect, or microcrystallization (local ordering) effect could influence, and maybe enhance, the magnitude of the PECD because of the subtle changes in the molecular potential "seen" by the outgoing scattered photoelectron. Besides such fundamental interest in terms of molecular photoionization dynamics, the probing of intermolecular effects involving chiral complexes is highly relevant to life sciences (*in vivo*) where (water) solvation and chiral (self-) recognition are basic fundamental biochemical processes.

Taking advantage of molecular beam techniques to control intermolecular interactions, we report here on a PECD experiment on clusters, using single pure homochiral camphor dimers (*RR*), for which the monomer valence-shell PECD is a well-documented showcase [9–12]; the dimer system may likewise serve as a benchmark. In addition, camphor proves to be an easy-to-handle, single-conformer, robust molecule, conveniently producing a limited distribution of cluster sizes (see Sec. III).

II. EXPERIMENTAL SETUP

The experimental setup is similar to the one used for our recent study of *endo*-borneol [17]. The experiment was conducted at the third-generation synchrotron facility Soleil (St Aubin, France) on the DESIRS vacuum-ultraviolet (VUV) beamline [24] with the permanently installed molecular beam chamber SAPHIRS. A commercial sample (98% pure, Aldrich) of the (1*R*)-(+) camphor enantiomer was placed in an in-vacuum oven and heated to 100 °C. The resulting vapor was mixed with helium acting as carrier gas at a variable pressure (0.5 to 3 bars) and expanded through a 50 μm pinhole. The supersonic expansion was skimmed through a 1.0 mm conical shape skimmer, before crossing the VUV photon beam at a right angle in the ionization chamber. The resulting ions and electrons were accelerated in opposite directions perpendicular to the molecular and photon beams inside the Delicious II angle-resolving photoelectron-photoion coincidence (ARPEPICO) imaging spectrometer [25].

This versatile spectrometer couples a modified velocity map imaging [26] (VMI) electron analyzer [27] with a Wiley-McLaren time-of-flight (TOF) ion mass spectrometer [28] and may be operated in electron-ion coincidence mode, so that angle-resolved photoelectron spectra (ARPES) on mass-selected species can be recorded, a feature necessary for the disentangling of the electron image contributions from the different clusters, as revealed by their TOF ion mass spectrum recorded in coincidence. The mass-selected PECD at each photon energy was measured by recording several mass-selected photoelectron images for alternate light helicities and then subtracting these to obtain a difference image, which was later treated using the PBASEX inversion algorithm [29] to recreate the original angular distribution of the difference. The full procedure and precautions to minimize purely instrumental effects have been described previously [11]. The apparatus is capable of imaging electrons with kinetic energies of up to 17 eV, with 5% resolving power, $E/\Delta E$, for the fastest electrons [27], associated with unit mass resolution up to ~200 amu. Energy calibration of the VMI spectrometer was performed by measurement of known rare gas photoelectron peaks made at selected photon energies [27].

Furthermore, slow electrons can be selectively imaged and detected by simply tuning the extraction field in DELICIOUS II to lower values, and so the ion spectroscopy can be accessed by measuring the threshold PES (TPES), with ultimate sub-meV resolutions [25]. When operated in coincidence mode, the spectrometer is capable of recording a TPES for a given mass or combination of masses in the TOF.

By reversing polarities, it is possible to operate DELICIOUS II in a cation imaging mode. This allows the optimization of the molecular beam conditions, such as the supersonic-to-thermal contribution or the cluster size distribution, by adjusting the *XYZ* position of the nozzle with respect to the skimmer, or the carrier gas backing pressure. In addition, for a given optimum beam condition, the translational energy distribution of a selected ion mass can be examined with any observed translational energy exceeding the beam temperature potentially revealing a preceding ion fragmentation process (i.e., dissociative ionization of a precursor species).

The experimental setup is installed in one of the two monochromatized branches available at the undulator-based DESIRS beamline which delivers left- and right-CPL over the whole experimental energy range (5–40 eV) with absolute circular polarization values of $|S_3| \geqslant 0.9$, as accurately

measured by a dedicated VUV polarimeter [30] located just upstream from the sample. These values of S_3 for the different photon energies are used for normalizing the PECD data. For the low photon energies used in the present paper, a gas filter [31] was filled with 0.25 mbar of argon to avoid high harmonics generated by the undulator that would be transmitted by the grating. We selected a low-dispersion (200 grooves/mm), high-flux grating ($\sim 10^{12}$–10^{13} photons per second in 0.1% bandwidth) mounted on the beamline's 6.65 m Eagle off-plane monochromator [32], offering a tunable resolving power of up to 4000. In practice, for the PECD measurements the resolution is limited by the kinetic energy (KE) resolution of the spectrometer in the ARPEPICO mode (except for very low KE), and therefore the entrance and exit slits were simply adjusted to avoid saturation of the detectors.

For the scanned wavelength studies (ionization yield scans, mass-selected TPES), the slits were set to provide a photon resolution of typically 5 meV around 9 eV, and a 2.5 meV step size was employed. The photon flux was monitored in real time by a dedicated photodiode (IRD, AXUV-100) mounted immediately behind the spectrometer, allowing for a proper normalization of all scans.

III. RESULTS AND DISCUSSION

A. Ion imaging and ion yields

We first optimized the jet conditions in order to produce a satisfactory distribution of cluster masses by observing the mass and momentum distribution in the ion imaging mode of DELICIOUS II. In this mode of operation, the VMI properties will be such that the different masses seeded in the sample beam, all traveling across through the source region with the same mean jet velocity, will be dispersed along the jet axis in the ion image, the heavier appearing further displaced on the position-sensitive detector (PSD) because of their longer TOF from ionization source to detector. Typical examples of such images, recorded at a photon energy of 8.80 eV, not far above the ionization potential (IP) of the monomer, are presented in Fig. 1.

In Fig. 1(a), recorded with a low backing pressure of helium (0.5 bars), only the camphor monomer contributions can be seen: a weak, diffuse thermalized background plus a clear, offset monomer peak. The beam speed could be estimated using the predetermined VMI energy calibration, hence giving $\langle v_{\text{beam}} \rangle \approx 350$ m s^{-1}, which corresponds to a Mach number of Ma = 0.35 (subsonic) and a beam temperature of $T_{\text{beam}} =$ 350 K for these particular beam conditions [33]. With such a hot beam the clusters are not expected to be formed, as confirmed in Fig. 1(a).

A different result is found with a higher backing pressure of 3 bars He. Now the distribution in Fig. 1(b) can be easily attributed to monomer, dimer, and trimer contributions whose impact position along the beam direction follows a $x_0 + \sqrt{m}$ law (where m is the mass and x_0 the position of the thermal molecules), as obtained from a crude model that neglects the inhomogeneous properties of the VMI spectrometer. Because of the more pronounced adiabatic expansion of the beam with the increased stagnation pressure, a higher beam speed ($\langle v_{\text{beam}} \rangle \approx 1740$ m/s, Ma = 11.1) can now be reached, corresponding to an estimated beam temperature of $\leqslant 10$ K, and leading to a cluster size distribution extending to heavier masses, as can clearly be observed in Fig. 1(b).

The energy resolution of the VMI spectrometer establishes an upper limit on any excess kinetic energy release that can be detected. Under the imaging conditions employed here, dissociative ionization processes yielding fragments with a translational excitation <2 meV will not be separated from the cold parent ions in the images. But, to within this sensitivity limit, the images shown in Fig. 1 show no evidence of translationally excited fragment masses formed by dissociative ionization.

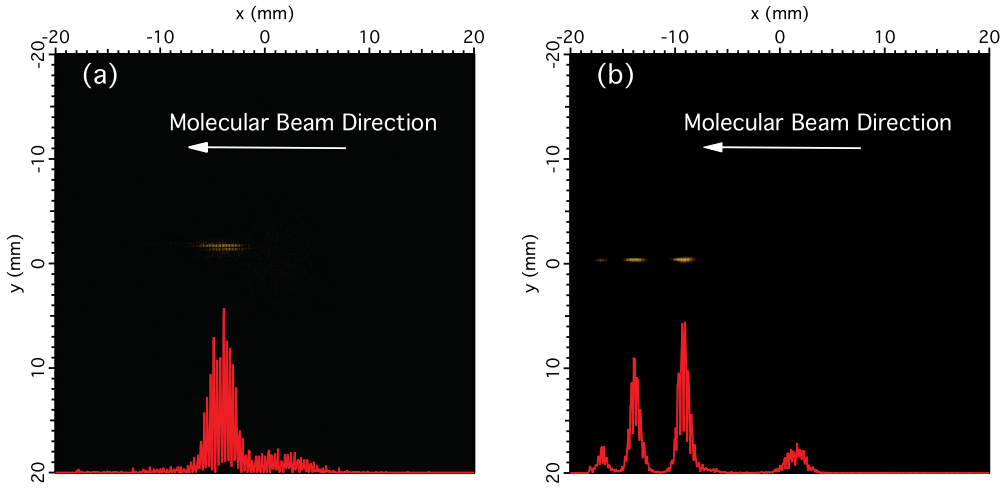

FIG. 1. (Color online) Photoion velocity map images of a camphor beam seeded in He recorded at $h\nu = 8.8$ eV for 0.5 bars (a) and 3 bars (b) of He backing pressure. Along the bottom of each image is shown the projection of ion distribution along the molecular beam direction, corresponding to the beam velocity distribution. This shows more clearly the diffuse, central, isotropic thermal background signal. At high backing pressure the lower temperature in the molecular beam favors the formation of clusters, as seen in (b), where the monomer, dimer. and trimer all appear, dispersed along the beam direction, in the image. The fine structure observed results from the 90% transmission mesh across the front detector face.

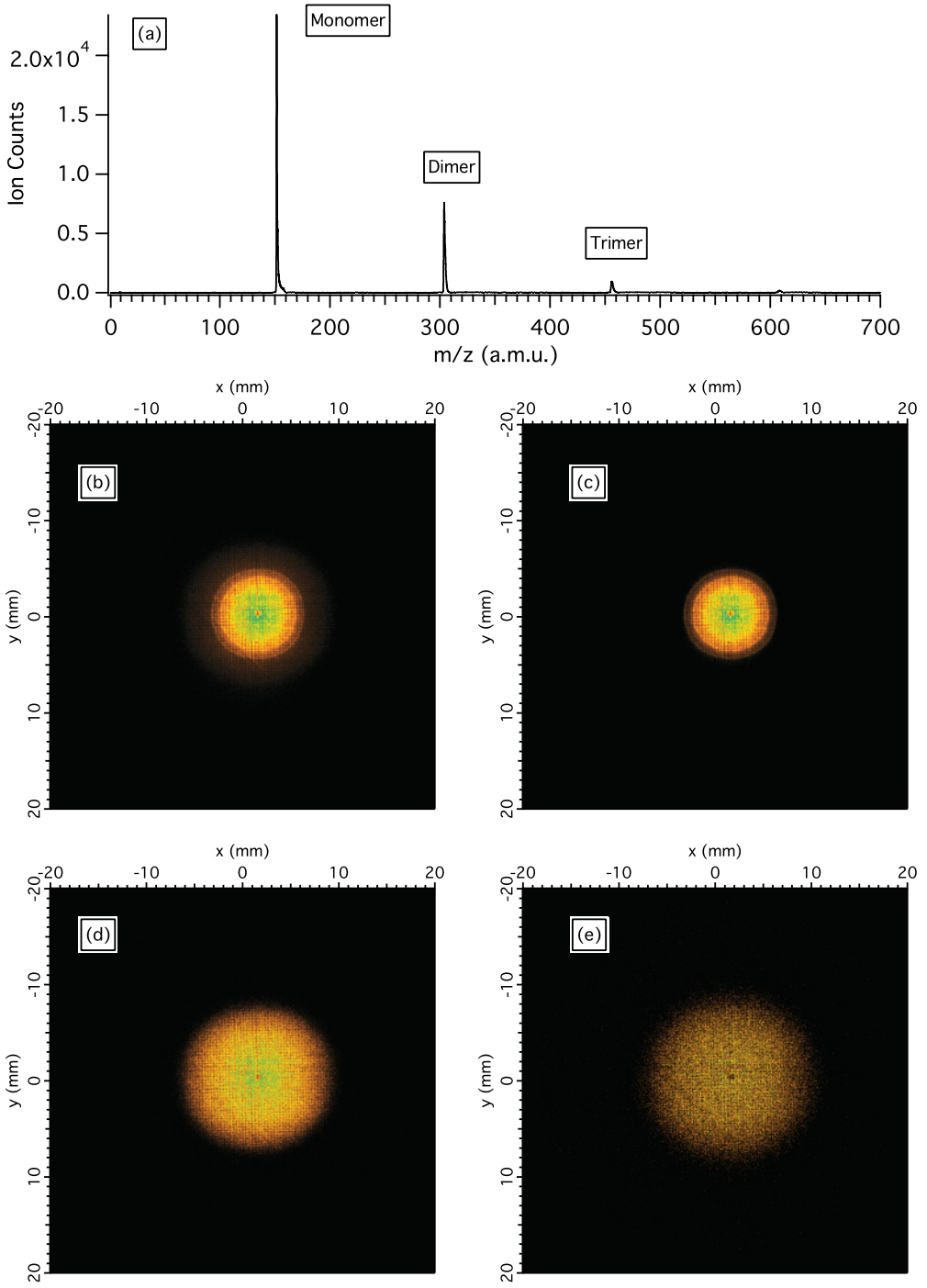

FIG. 2. (Color online) PEPICO measurements recorded at 8.80 eV with right-handed CPL on camphor seeded in He (3 bars). (a) Mass spectrum; (b) raw total electron image; (c)–(e) Mass-filtered raw electron images corresponding, respectively, to the monomer, dimer, and trimer. The size of the mass-selected images (c)–(e) increases due to the progressive lowering of the cluster IPs (see text for details).

Although from Fig. 1(b) we clearly observe the cluster population decreasing with heavier masses, saturation effects on the microchannel plate detector due to the tight focusing of the ion beam prevent us from giving quantitative branching ratios from the ion images. Nevertheless, we show from the ion imaging that we can manipulate the beam conditions so as to optimize the cluster size distribution. In the following we use and compare two beam expansion conditions: the "cold" 10 K cluster beam formed with 3 bars He stagnation pressure, and a "warm," nonclustering beam formed with 0.6 bars He, for which we will infer a vibrational temperature of 300 K (*vide infra*).

By switching to the PEPICO mode of operation of DELICIOUS II, we are able to record electron images and ion mass spectra in coincidence. The data obtained in such a PEPICO measurement with the cluster beam and at a photon energy of 8.8 eV are shown in Fig. 2. From the TOF spectrum shown in Fig. 2(a) we can get a more

quantitative cluster size distribution in the jet since, at least at this photon energy, there are no fragmentation processes and no saturation in the TOF detector, and we checked that the spectrometer does not discriminate against high masses by varying the extraction field. Therefore, a reasonably flat overall transmission versus mass may be assumed, which is the case for quite large molecular systems [34], since the transmission effects of the skimmer and of the ion TOF microchannel plate (MCP) detectors are self-compensating. Hence, we can deduce from Fig. 2(a) that the amount of trimer ion (456 amu) is quite negligible and that the dimer ion (304 amu) population is of the order of 20% of the monomer ion (152 amu) at 8.8 eV. Similar conclusions hold at higher photon energies studied, up to 9.2 eV. Only at 10.3 eV and above, where the HOMO-1 ionization is accessible, do we see fragmentation to submonomer masses, and the PEPICO data confirm that this fragmentation is solely from the electronically excited ion.

In Fig. 2(b) is presented the corresponding complete $h\nu = 8.8$ eV electron image, which can be decomposed into its mass-filtered components as presented in Figs. 2(c), 2(d), and 2(e) for, respectively, the monomer, dimer, and trimer nascent species. These latter three images show increasing radius with increasing masses, and hence an increasing maximum electron kinetic energy, corresponding to a decrease of the IPs with increasing coincident ion mass. This lowering of IPs with increasing cluster size is not surprising as it is quite typically observed, for instance in the photoionization of acetone cluster systems [35]. The phenomenon corresponds to a stabilization of the complex in the ion as compared to the neutral, because of the larger charge-dipole interaction in the ionic form.

Wavelength scans of the near-threshold region were recorded in PEPICO mode. No energy selection was applied to the electrons, but they were used to start the ion timing circuitry for recording TOF spectra. The mass-selected ion counts are thus essentially photoion yield curves. These ion yield curves, obtained under the strong clustering conditions identified above (3 bars He backing pressure), are shown in Fig. 3. The cooled monomer has an onset around ~8.65 eV while the dimer ion yield is, as anticipated, shifted to lower threshold in the ~8.4 eV region. Correspondingly, the trimer ion threshold evidently extends down to ~8.3 eV.

However, closer examination of the dimer and trimer threshold behavior (left inset, Fig. 3) reveals a more complicated behavior. Here it is seen that, when plotted on the same magnified absolute intensity scale, the dimer and trimer yields below 8.38 eV are commensurate, and apparently share the same threshold, within the sensitivity of our measurements. It seems very probable that in this region a proportion of the neutral trimers (or even any higher n-mers), when ionized, are fragmenting leading to the appearance of dimer ion. The observed common onset $\leqslant 8.30 \pm 0.01$ eV is thus attributed to the ionization and/or dissociative ionization threshold of the trimer (or higher n-mer) neutral clusters.

On the other hand, above 8.38 eV the slope of the dimer yield curve rapidly increases, and the yield rapidly exceeds that of the trimer. By extrapolating a least squares fit of the steeper, linear region between 8.38 and 8.48 eV back to its intercept with the baseline, we obtain a higher, second dimer ion threshold estimate of 8.37 ± 0.01 eV, which we take to be indicative of the nascent neutral dimer's ionization potential.

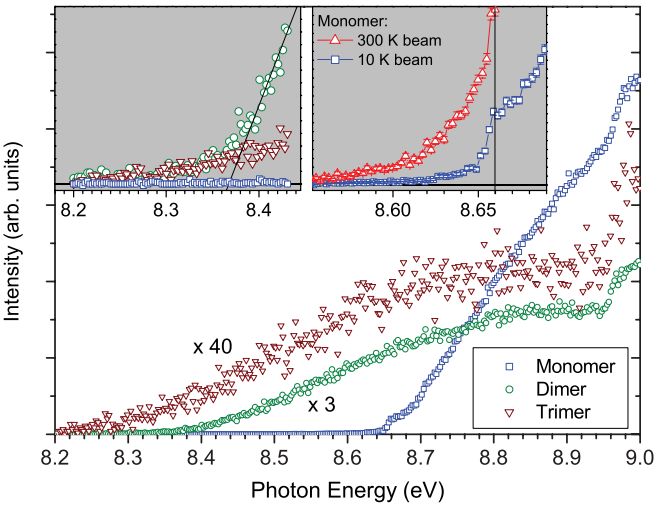

FIG. 3. (Color online) Ion yield curves for monomer, dimer, and trimer ions, recorded in a cold, supersonic beam (10 K, 3 bars He backing pressure). The ion counts are normalized to photon flux and scaled as shown. The two insets provide expanded views of the monomer and cluster threshold regions. The latter compares monomer, dimer, and trimer yields on the same scale and includes a fitted straight line extrapolation of the higher-energy region of the dimer curve to the baseline (see text). The former includes a comparison of the monomer threshold behavior observed in a warm, nonclustering beam (300 K, 0.6 bars He backing pressure).

Throughout this cluster threshold region the monomer yield curve remains flat along the zero-count baseline, so there are no comparable indications to suggest formation of monomer ion from ionization of camphor n-mers ($n = 2, 3, \ldots$). The first rise of the monomer ion signal from the baseline occurs as a sharp step onset, centered at 8.66 ± 0.01 eV, which can be identified as the monomer adiabatic IP. The narrow width of this step function (half width at half maximum ~15 meV before deconvoluting the instrumental bandwidth) attests to the cooling achieved by these expansion conditions, since a rotational envelope of ~40 meV ($= \frac{3}{2}kT$) could be expected at room temperature. This is additionally evident in comparison with the monomer threshold behavior observed with the warmer (300 K), nonclustering camphor beam conditions as shown in the right inset to Fig. 3. In these conditions the adiabatic step rise is smeared out and the experimental onset spreads to some 50 meV lower, as would be anticipated in the presence of hot band contributions.

There is a further significance to be seen in this comparison of monomer ion threshold behavior. Were some of the monomer ion seen in the clustering beam conditions to result from dissociative ionization of higher n-mers, then the monomer ion appearance energy would be expected to tail to *lower* ionization energy under clustering beam conditions because of the lower IPs of any contributing cluster channels. In fact the apparent monomer ion threshold shifts to *higher* ionization energy under these conditions, as the lower internal energy achieved in the cooler beam causes an approach toward the true adiabatic onset.

We thus infer that across this near-threshold region the monomer ion results solely from ionization of the neutral monomer and the dimer ion results predominantly from ionization of the neutral dimer, with a negligibly small contribution from dissociative ionization of higher clusters when above the 8.37 eV dimer IP. As one progresses to higher ionization energies, a greater degree of fragmentation of the nascent ionized n-mers might be anticipated. However, the ion imaging measurements (for example at $h\nu = 8.8$ eV, Fig. 2) show no evidence for any excess translational energy (to within the 2 meV sensitivity limit noted above) that could be expected to accompany formation of ions via fragmentation of higher n-mers. It should also be noted, at least for these specific camphor systems, that on statistical grounds very little excess energy would be expected to be partitioned into translation [the monomer unit having 75 ($=3N-6$) vibrational modes to sink energy], so that a negative observation as reported is not so conclusive. But by the same reasoning camphor n-mers should be slow to dissociate, and hence be kinetically stable, even well above their thermodynamic binding energies.

In summary, we infer from the above data that mass selection on the monomer and dimer ions achieves a very high degree of size selection on the corresponding nascent neutral precursors. Because of the low intensity of the trimer ion near threshold and its negligible contribution elsewhere, we henceforth focus on the two lighter species.

B. Threshold photoelectron spectroscopy

Figure 4 shows the mass-selected HOMO band TPES of camphor monomer, recorded in the clustering (10 K) and nonclustering (300 K) beam conditions together with, for comparison, a previous PES [36] recorded in a 350 K gas cell. The additional vibrational structure revealed in the cold beam is striking, and this has been analyzed with a 10 K double-harmonic parallel-mode approximation simulated spectrum (using the program EZSPECTRUM [37]) employing B3LYP/cc-pVDZ harmonic frequencies calculated with GAUSSIAN03 [38] to which a 0.97 scaling factor [39] has been applied. The resulting stick spectrum has finally been convoluted with an 8-meV-wide Gaussian function to facilitate direct comparison with the cold experimental spectrum, as indicated in Fig. 4.

The simulated spectrum convincingly reproduces at least the first five distinct peaks in the cold experimental TPES. In particular the first prominent peak is readily assigned to the 0-0 origin, confirming the identification of the adiabatic IP at 8.66 eV. It may be noted that simulated intensities are based on computed Franck-Condon factors, although the complex nature of the threshold ionization mechanism [40,41] means that TPES intensities frequently deviate from a Franck-Condon envelope; therefore exact matching of intensities is not necessarily expected. The 8 meV Gaussian width chosen to match simulated peaks to the experiment is barely more than the convolution of the estimated 5 meV electron resolution and 5 meV photon resolution, confirming the high degree of rotational cooling in the cold beam expansion. Nevertheless, even in the cold TPES, a weak feature (8.63 eV) appears below the adiabatic threshold (although not in the 10 K simulation); this we take to be a hot band from a vibrational level(s) resistant to cooling in the beam expansion. The position,

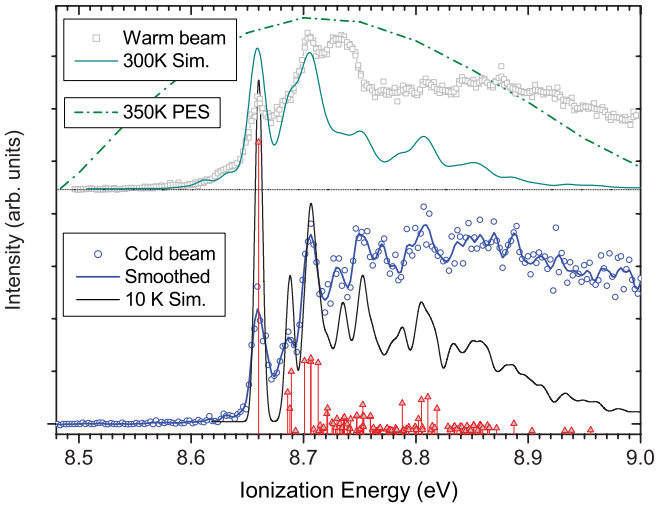

FIG. 4. (Color online) TPES of the HOMO band of the camphor monomer. The lower spectrum was recorded under cold, cluster beam conditions, while the upper spectrum was recorded for a warm, nonclustering beam. A smoothed curve is added through the lower spectrum to guide the eye. Simulated spectra (see text) calculated at, respectively, 10 and 300 K are overlaid. The lower panel also includes a stick spectrum showing positions and relative intensities of the more intense calculated excitations. This is omitted for the upper panel due to congestion from the many additional hot band transitions, but a lower-resolution PES recorded in a 350 K gas cell is included for comparison (from Ref. [36]).

~30 meV below the origin, suggests that this may be one or more of the modes associated with the second major TPES peak similarly displaced ~30 meV above the origin, since the $v_0 \leftrightarrow v_1$ Franck-Condon factors are seen to be favorable for these. Of the three most prominent low-frequency modes that are predicted to contribute $v_0 \rightarrow v_1$ transitions immediately above the origin band (and so are potentially contributing to a $v_1 \rightarrow v_0$ hot band falling below the origin), two are essentially methyl group torsional modes, and one a skeletal deformation.

The second TPES in Fig. 4, recorded in the warmer, nonclustering beam conditions, shows certain differences, including the anticipated tailing toward a lower onset consistent with contributions from hot band ionization. This is confirmed with a second simulation where we have increased the temperature to 300 K and the peak width to 15 meV. (We note that a 350 K simulation overestimates the hot band intensities, confirming the additional cooling in the 0.6 bar He expansion.) Now there are two multicomponent hot band structures that appear at ionization energies below the adiabatic origin peak, the first of which also correlates with the 8.63 eV feature noted in the cold beam above and postulated to be inefficiently cooled thermal vibration. The most prominent contributions to this hot band in the 300 K simulations come from $\Delta v = -1$ transitions from levels having one or two quanta of the same methyl group torsions and skeletal deformation as already identified. One also sees that the previously determined [36] vertical ionization energy of 8.70 eV, obtained at much lower 300 meV resolution in a 350 K gas cell, is fully consistent with the envelope of the warm beam TPES.

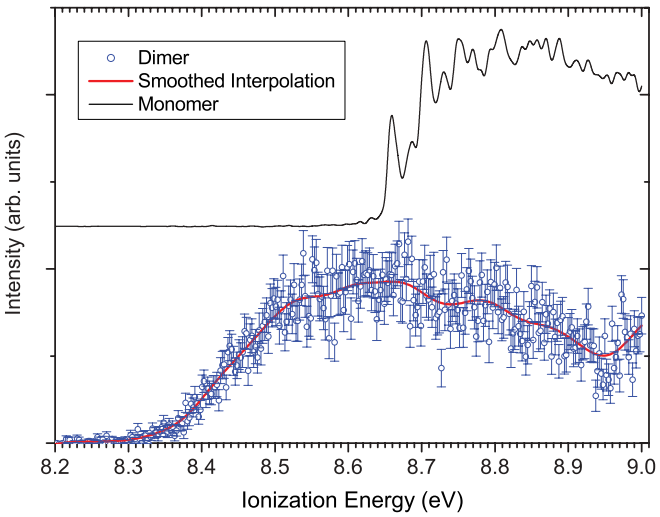

FIG. 5. (Color online) Experimental dimer TPES compared with that of the monomer (as in Fig. 4) recorded in the same 10 K beam.

The dimer TPES is shown in Fig. 5. The signal-to-noise ratio is less than that of the monomer spectrum owing to a lower yield of dimer in the beam conditions. For the spectrum shown, the effective TPES electron energy resolution has been downgraded in the data analysis stages [25] to 30 meV, with some statistical benefits, but we have examined resolution ranging from 5 to 50 meV with the same conclusions. Two characteristics are always evident: first the substantial shift to a lower ionization potential than the monomer, as discussed in connection with the ion yield curves above; second, a complete lack of any vibrational structure comparable to the monomer TPES. Note the perfectly flat spectrum of the monomer in this region below 8.60 eV, firmly attached to the zero baseline, showing again no spurious contributions from dissociating dimers.

The high intensity of the origin band in the monomer indicates that the geometries of the ion and of the neutral are quite similar (which makes sense considering that the HOMO orbital is mainly based upon the carbonyl O lone pair, nonbonding orbital). The contrasting shallow onset and weak, unstructured dimer TPES may most likely be explained by a substantial equilibrium geometry change occurring on ionization of the dimer. A similar observation and deduction have been presented in a previous photoionization study of acetone and its dimer [35], which is somewhat analogous.

To develop this argument, we show in Fig. 6 a likely structure for the camphor dimer. This structure was optimized from two *R*-camphor enantiomer structures in CHARMM, using the Molecular Mechanical Force Fields 94 (MMFF94) force field [42]. The key feature is the electrostatically favorable antiparallel arrangement of the two $C = O$ dipoles, with additional intermolecular H bonding. A very similar structure has been inferred from IR investigation of the acetone dimer [43] and was predicted in a detailed theoretical investigation of the acetone dimer potential [44]. In both acetone and camphor monomers the HOMO is essentially a nonbonding carbonyl lone pair electron, so that it is likely its removal via ionization will have only limited impact on the respective monomer ion geometry, as inferred. However, it is equally plausible that the

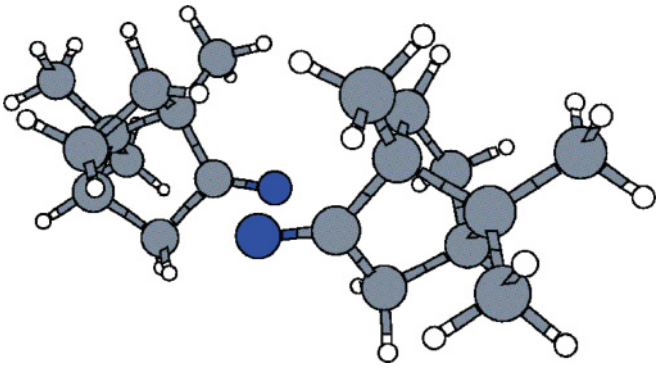

FIG. 6. (Color online) Optimised structure for camphor dimer, showing anti-parallel stacking of the $C = O$ dipoles.

additional charge adjacent to a dipole in one of the dimer ions would significantly perturb the equilibrium geometry and lead to a significantly greater interaction between the monomer units, as already inferred from the significant IP shifts (several hundred meV) seen for both systems.

C. Photoelectron angular distributions and PECD

Arguments presented in the preceding sections demonstrate very clearly that the ion mass selection applied to the ionization data corresponds very closely to a size selection imposed upon the nascent neutral cluster. We are thus able to examine differences in the spectroscopy, and crucially the photoelectron angular distribution parameters of the dimer as compared to the cold monomer species. As an example of the treated data that can be obtained from the mass-selected electron images, such as in Fig. 2, we present in Figs. 7(a) and 7(b), for the

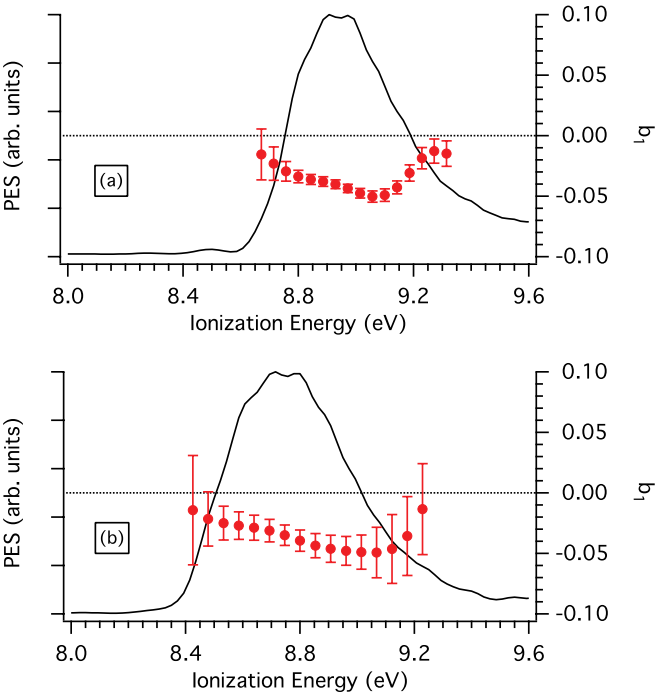

FIG. 7. (Color online) PES (solid curves) and chiral b_1 values (points) for the HOMO orbital of the monomer (a) and dimer (b) of *R*-camphor obtained by PEPICO mass-selected velocity map electron imaging, recorded at 10.3 eV photon energy.

monomer and dimer channels respectively, the mass-selected PES and chiral b_1 values recorded at 10.3 eV photon energy.

Again, just as with the earlier TPES, we can see from the $h\nu = 10.3$ eV PES that the monomer channel is not "polluted" by any dimer ion fragmentation contribution that would lead to a low-binding-energy tail on the monomer HOMO PES. This is clearly absent, the monomer PES mimicking the monomer-selected TPES presented in Fig. 4, of course convolved with the lower resolution of the VMI spectrometer in the "fast electron" mode. As for the b_1 values, they show some variations in the HOMO vibrational envelope, probably due to some vibronic effects on the PECD, which we do not fully resolve but which appear different in the monomer and dimer. To form an overview of the variation of the angular distribution parameters we proceed to compare measurements for both the nascent monomer (*R* enantiomer) and dimer (*RR* complex) recorded at five photon energies from 8.6 to 10.3 eV. For each photon energy we plot in Fig. 8 mean parameter values for both β and b_1 that each represent an average, weighted by the PES intensity, over the full width at half maximum of the HOMO vibrational envelope for the selected species.

In Fig. 8(a) we present a summary of the b_2 angular parameters versus electron kinetic energy, which in the case of

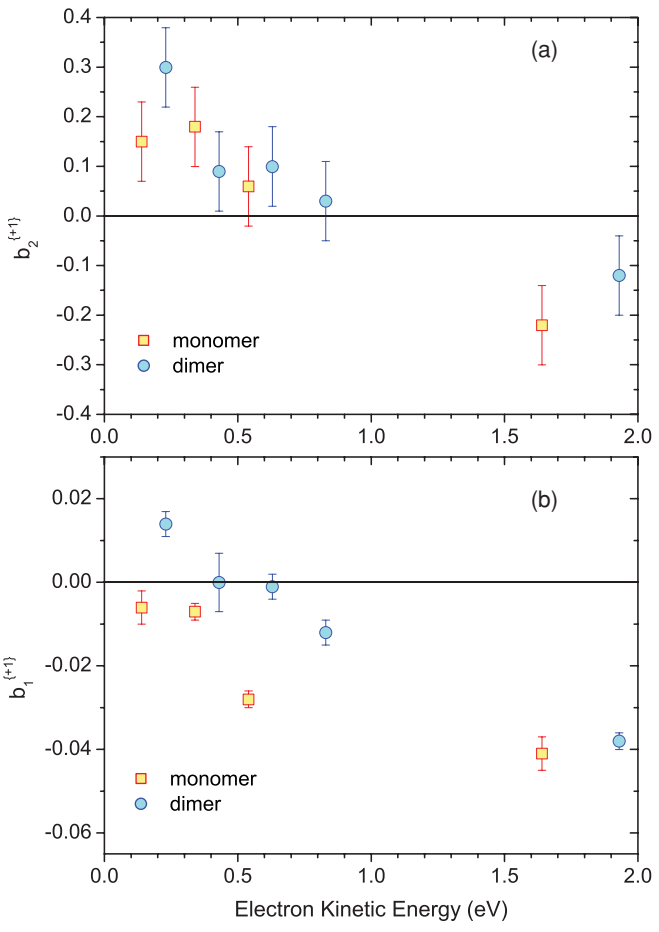

FIG. 8. (Color online) Mean HOMO band angular parameters: (a) $b_2^{[\pm1]}$ $[=-(1/2)\beta]$; (b) $b_1^{\{+1\}}$ recorded for the *R*-(+) camphor monomer and *RR* homodimer, presented as a function of electron kinetic energy.

CPL correspond to $-(1/2)\beta$ where β is the usual anisotropy parameter. The dimer points recorded at a given photon energy are offset from the corresponding monomer values by the observed difference in IP of the two species. Clearly, however, within the displayed error bars, the b_2 curves for the monomer and dimer are similar, and do not themselves serve to distinguish the cluster size.

In contrast, Fig. 8(b) shows that the monomer and dimer have distinctively different chiral b_1 asymmetry parameters with the dimer even undergoing a sign change over the studied KE range. Over the same range of electron energy, the monomer b_1 value is uniformly negative, with an increasing magnitude from threshold to about $h\nu = 10$ eV (KE 1.34 eV) as previously observed [11]. This distinctive dimer behavior is consistent with the fact that PECD appears to be a fine probe of the whole molecular structure, especially for slow photoelectrons which are able to "sample" small variations in the molecular potential as in a "slow electron scattering from within" experiment. Note that such a higher sensitivity of slow photoelectrons to molecular structures has already been observed in the case of *endo*-borneol monomer conformers [17].

IV. CONCLUSIONS AND FUTURE PROSPECTS

Owing to the use of different spectroscopic and imaging approaches, we have been able in this article to show that for camphor the mass selection achieved in a PEPICO scheme does correspond to a size selection of the nascent species, monomer and dimer. Taking advantage of this, we were able to initiate studies of the valence-shell angular distribution of photoelectrons from size-selected molecular dimers. A real bonus, and one of the major motivations for this work, is that the monomer and dimer are chiral, so that the angular distributions have to be described not only by the usual β parameter, but also by a second chiral asymmetry parameter b_1.

We find in this study that the traditional anisotropy parameter β appears to be insensitive to dimerization. Interestingly, the same conclusion was reached in an investigation of $2p^{-1}$ photoionization of Ar and Ar_2 [4]. One cannot, of course, generalize this conclusion regarding β from just two limited studies, yet it does clearly point up an advantage of having the second chiral b_1 parameter for study in the present case, since this does show a clear size dependence. This is as anticipated from previous PECD investigations that have revealed the more marked structural dependence of b_1, consequent upon its enhanced sensitivity to phase shifts in the outgoing electron partial wave expansion [7,18].

Nevertheless, the absolute magnitudes in these low-energy monomer and dimer b_1 curves for camphor are not so very different, and we do not observe here the significant enhancement of the PECD in the dimer that might be anticipated due to some caging or micro-crystallization effect. It is possible, in this case, that several homogeneous *RR* dimer conformers are present in the jet. Their individual b_1 values, which may *a priori* range positive and negative, could then tend to average out, leading to a lower absolute value than the b_1 of a single dimer conformation. Such a lowering resulting from a conformer averaging effect has been observed in the case of *endo*-borneol monomer [17]. Therefore, we cannot form

a definitive conclusion on the likelihood of such anticipated PECD enhancements from the present study alone.

We wish to pursue such studies in the future on systems for which the dimerization conformation is well documented by spectroscopic techniques and presents a single dominant conformer, as for instance in the case of glycidol dimers [45–47]. This would allow one to see a possible enhancement of the dimer PECD without any potential countering from conformer averaging. This would also pave the way for future studies on chiral recognition in gas phase heterodimers, for which "the molecular handshake" electronic structure could be probed by a direct chiroptical method, by comparing the PECD measured in two separated experiments targeted onto the A_RB_R and A_RB_S complexes. There, A and B are two different monomers with different masses so that the AA, BB, and AB complexes can be disentangled by their masses in our PEPICO scheme.

This work also introduces the methodology for future work on PECD measurements on more general studies involving H-bonding interaction, of great interest in life science, especially when involving chiral systems and water.

ACKNOWLEDGMENTS

We are indebted to the general technical staff of the SOLEIL synchrotron for running the facility. We would like to warmly thank Jean-François Gil for technical help and for designing a new version of the in-vacuum oven. V. A. Mozhayskiy very kindly helped adapt the EZSPECTRUM codes to deal effectively with the challenges created by such a large chiral system.

[1] R. L. Johnston, *Atomic and Molecular Clusters* (Taylor & Francis, London, 2002).
[2] M. Kappes and S. Leutwyler, in *Atomic and Molecular Beam Methods, Part 1*, edited by G. Scoles (Oxford University Press, New York, Oxford, 1988), p. 380.
[3] K. L. Reid, Annu. Rev. Phys. Chem. **54**, 397 (2003).
[4] A. De Fanis, M. Oura, N. Saito, M. Machida, M. Nagoshi, A. Knapp, J. Nickles, A. Czasch, R. Dorner, Y. Tamenori, H. Chiba, M. Takahashi, J. H. D. Eland, and K. Ueda, J. Phys. B **37**, L235 (2004).
[5] T. Jahnke, A. Czasch, M. Schoffler, S. Schossler, M. Kasz, J. Titze, K. Kreidi, R. E. Grisenti, A. Staudte, O. Jagutzki, L. P. H. Schmidt, S. K. Semenov, N. A. Cherepkov, H. Schmidt-Bocking, and R. Dorner, J. Phys. B **40**, 2597 (2007).
[6] D. Rolles, H. Zhang, Z. D. Pesic, J. D. Bozek, and N. Berrah, Chem. Phys. Lett. **468**, 148 (2009).
[7] I. Powis, in *Advances in Chemical Physics*, edited by J. C. Light (Wiley, New York, 2008), Vol. 138, p. 267.
[8] U. Hergenhahn, E. E. Rennie, O. Kugeler, S. Marburger, T. Lischke, I. Powis, and G. Garcia, J. Chem. Phys. **120**, 4553 (2004).
[9] T. Lischke, N. Böwering, B. Schmidtke, N. Müller, T. Khalil, and U. Heinzmann, Phys. Rev. A **70**, 022507 (2004).
[10] G. A. Garcia, L. Nahon, M. Lebech, J. C. Houver, D. Dowek, and I. Powis, J. Chem. Phys. **119**, 8781 (2003).
[11] L. Nahon, G. A. Garcia, C. J. Harding, E. A. Mikajlo, and I. Powis, J. Chem. Phys. **125**, 114309 (2006).
[12] M. Stener, D. D. Tommaso, G. Fronzoni, P. Decleva, and I. Powis, J. Chem. Phys. **124**, 024326 (2006).
[13] S. Stranges, S. Turchini, M. Alagia, G. Alberti, G. Contini, P. Decleva, G. Fronzoni, M. Stener, N. Zema, and T. Prosperi, J. Chem. Phys. **122**, 244303 (2005).
[14] S. Turchini, D. Catone, G. Contini, N. Zema, S. Irrera, M. Stener, D. D. Tommaso, P. Decleva, and T. Prosperi, Chem. Phys. Chem. **10**, 1839 (2009).
[15] A. Giardini, D. Catone, S. Stranges, M. Satta, M. Tacconi, S. Piccirillo, S. Turchini, N. Zema, G. Contini, T. Prosperi, P. Decleva, D. Di Tommaso, G. Fronzoni, M. Stener, A. Filippi, and M. Speranza, Chem. Phys. Chem. **6**, 1164 (2005).
[16] G. A. Garcia, L. Nahon, C. J. Harding, and I. Powis, Phys. Chem. Chem. Phys. **10**, 1628 (2008).
[17] G. A. Garcia, H. Soldi-Lose, L. Nahon, and I. Powis, J. Phys. Chem. A **114**, 847 (2010).
[18] C. J. Harding and I. Powis, J. Chem. Phys. **125**, 234306 (2006).
[19] M. Stener, G. Fronzoni, D. Di Tommaso, and P. Decleva, J. Chem. Phys. **120**, 3284 (2004).
[20] I. Powis, C. J. Harding, G. A. Garcia, and L. Nahon, Chem. Phys. Chem. **9**, 475 (2008).
[21] L. Nahon and I. Powis, in *Chiral Recognition in the Gas Phase*, edited by A. Zehnacker (Taylor & Francis, Boca Raton, FL, 2010).
[22] J. Paul, A. Dorzbach, and K. Siegmann, Phys. Rev. Lett. **79**, 2947 (1997).
[23] J. Paul and K. Siegmann, Chem. Phys. Lett. **304**, 23 (1999).
[24] [http://www.synchrotron-soleil.fr/portal/page/portal/Recherche/LignesLumiere/DESIRS].
[25] G. A. Garcia, H. Soldi-Lose, and L. Nahon, Rev. Sci. Instrum. **80**, 023102 (2009).
[26] A. T. J. B. Eppink and D. H. Parker, Rev. Sci. Instrum. **68**, 3477 (1997).
[27] G. A. Garcia, L. Nahon, C. J. Harding, E. A. Mikajlo, and I. Powis, Rev. Sci. Instrum. **76**, 053302 (2005).
[28] W. C. Wiley and I. H. Maclaren, Rev. Sci. Instrum. **26**, 1150 (1955).
[29] G. A. Garcia, L. Nahon, and I. Powis, Rev. Sci. Instrum. **75**, 4989 (2004).
[30] L. Nahon and C. Alcaraz, Appl. Opt. **43**, 1024 (2004).
[31] B. Mercier, M. Compin, C. Prevost, G. Bellec, R. Thissen, O. Dutuit, and L. Nahon, J. Vac. Sci. Technol. A **18**, 2533 (2000).
[32] L. Nahon, C. Alcaraz, J. L. Marlats, B. Lagarde, F. Polack, R. Thissen, D. Lepère, and K. Ito, Rev. Sci. Instrum. **72**, 1320 (2001).
[33] D. R. Miller, in *Atomic and Molecular Beam Methods, Part 1* (Ref. [2]), p. 14.
[34] B. Gans, L. Vieira Mendes, S. Boyé-Peronne, S. Douin, G. Garcia, H. Soldi-Lose, B. Cunha de Miranda, C. Alcaraz, P. Pernot, N. Carrasco, and D. Gauyacq, J. Phys. Chem. A **114**, 3237 (2010).

[35] W. M. Trott, N. C. Blais, and E. A. Walters, J. Chem. Phys. **69**, 3150 (1978).
[36] E. E. Rennie, I. Powis, U. Hergenhahn, O. Kugeler, G. Garcia, T. Lischke, and S. Marburger, J. Electron Spectrosc. Relat. Phenom. **125**, 197 (2002).
[37] V. A. Mozhayskiy and A. I. Krylov [http://iopenshell.usc.edu/downloads].
[38] M. J. Frisch, computer code GAUSSIAN, Gaussian Inc., Wallingford, CT, 2005.
[39] J. P. Merrick, D. Moran, and L. Radom, J. Phys. Chem. A **111**, 11683 (2007).
[40] P. M. Guyon, T. Baer, and I. Nenner, J. Chem. Phys. **78**, 3665 (1983).
[41] T. Baer and P. M. Guyon, in *High Resolution Laser Photoionization and Photoelectron Studies*, edited by I. Powis, T. Baer, and C.-Y. Ng (John Wiley & Sons, London, 1995), p. 1.
[42] J. D. Hirst and J. Melville (private communication).
[43] Y. Matsuda, K. Ohta, N. Mikami, and A. Fujii, Chem. Phys. Lett. **471**, 50 (2009).
[44] J. M. Hermida Ramon and M. A. Rios, J. Phys. Chem. A **102**, 2594 (1998).
[45] A. Maris, B. M. Giuliano, D. Bonazzi, and W. Caminati, J. Am. Chem. Soc. **130**, 13860 (2008).
[46] N. Borho and M. A. Suhm, Phys. Chem. Chem. Phys. **4**, 2721 (2002).
[47] N. Borho, T. Haber, and M. A. Suhm, Phys. Chem. Chem. Phys. **3**, 1945 (2001).